CHINESE OPTICS LETTERS

Vol. 21, No. 3 | March 2023

Cylindrical vector beam generator on photonic crystal cavity integrated with metal split ring nanoresonators

Yingke Ji (姬应科)[1], Xin Xie (谢 鑫)[1*], Liang Fang (方 亮)[1**], Yisong Zhu (朱奕松)[2], Jianlin Zhao (赵建林)[1], and Xuetao Gan (甘雪涛)[1]

[1] Key Laboratory of Light-Field Manipulation and Information Acquisition, Ministry of Industry and Information Technology, and Shaanxi Key Laboratory of Optical Information Technology, School of Science and Technology, Northwestern Polytechnical University, Xi'an 710129, China

[2] Institute of Fundamental and Frontier Sciences, University of Electronic Science and Technology of China, Chengdu 610054, China

*Corresponding author: xinxie@nwpu.edu.cn

**Corresponding author: fangliang@nwpu.edu.cn

Received September 7, 2022 | Accepted October 25, 2022 | Posted Online November 15, 2022

We propose a chip-integratable cylindrical vector (CV) beam generator by integrating six plasmonic split ring resonators (SRRs) on a planar photonic crystal (PPC) cavity. The employed PPC cavity is formed by cutting six adjacent air holes in the PPC center, which could generate a CV beam with azimuthally symmetric polarizations. By further integrating six SRRs on the structure defects of the PPC cavity, the polarizations of the CV beam could be tailored by controlling the opening angles of the SRRs, e.g., from azimuthal to radial symmetry. The mechanism is governed by the coupling between the resonance modes in SRRs and PPC cavity, which modifies the far-field radiation of the resonance mode of the PPC cavity with the SRR as the nano-antenna. The integration of SRRs also increases the coupling of the generated CV beam with the free-space optics, such as an objective lens, promising its further applications in optical communication, optical tweezer, imaging, etc.

Keywords: vector beams; photonic crystal; plasmonics; integrated photonics.

DOI: 10.3788/COL202321.033601

1. Introduction

The cylindrical vector (CV) beam has the inhomogeneous polarization state and doughnut-like intensity distribution[1–4], promising a variety of interesting applications, including laser processing[5], superresolution imaging[6,7], phase contrast microscopy[8], and entanglement of the orbital angular momentum (OAM) state[9]. Generating CV beams on photonic chips is attractive. Compared with the generation techniques of CV beam in free-space optical systems, which requires several separate diffractive optics elements and their careful alignments, the on-chip CV beam generator is more compact, stable, and potentially large-scale manufacturable. Chip-integrated CV beam generators have been demonstrated based on microring resonators, grating arrays, and plasmonic nano-antenna arrays[10–12]. On-chip quantum computation with the CV beams processing OAM qudit states was proposed, which also has the ability of qudit sorters[11]. More recently, the CV beam has been utilized to excite the optical radiationless anapole hidden in a resonant state of a silicon nanoparticle[13].

The planar photonic crystal (PPC), as one of the desirable photonic integration architectures, enables the control of optical propagation and light–matter interaction in the wavelength-scale[14-16]. With their controllable photonic band structures, PPCs allow more reliable manipulations of light phases and polarization states via its Bloch modes, band-edge modes, and defect modes[17], which therefore provide a promising platform to develop CV beam generators. For instance, Noda *et al.* reported CV beam lasers relying on the bound states at the band edge of PPCs[18]. In our previous work, by removing or shaping the unit cells in a PPC to form the PPC cavities, azimuthally or radially polarized CV beams with different topological charges were realized[19,20]. However, due to the few numbers of Bloch or cavity modes, only typical CV beams with radial and azimuthal polarizations can be obtained[21]. It is still a challenge to arbitrarily manipulate the polarization state of CV beams in the PPC.

In this work, we propose an approach to generating CV beams with tunable polarization and intensity distribution, by integrating six plasmonic split ring resonators (SRRs) on a PPC cavity with multiple defects. By controlling the opening angles of the SRRs, the CV beams with varying polarization states and intensities are demonstrated. Owing to the coupling between the resonance modes in the SRRs and PPC cavity, the collection efficiency of the CV beam is significantly improved compared to the bare PPC cavity. The tailorable polarizations and high collection efficiency of the generated CV beam could certify the SRR-PPC cavity as a promising on-chip CV beam generator.

2. Generation of CV Beams in a PPC Cavity

To obtain a perfect CV beam, we construct a symmetric structure to form a PPC cavity based on six D-type cavities in the silicon PPC slab. As shown in Fig. 1(a), the defects in PPC slab are introduced by cutting of six adjacent air holes in the PPC center. Here, the PPC slab has a thickness of $t = 220$ nm and lattice constant of $a = 370$ nm; the radius of the hole is $r = 0.34\,a$, corresponding to the resonant wavelength around 1000 nm. Figure 1(b) shows the resonance mode of the PPC cavity, presenting strong confinement of light in the six defects. The quality (Q) factor of the resonance mode is 1089. Moreover, this cutting-defect structure enables its mode volume V_m to be low as $0.72(\lambda/n_{\text{slab}})^3$. The ultrahigh Q/V_m factor could promise strong light–matter interaction in the PPC cavity, which could facilitate the lasing behavior and nonlinear optical processes of the CV beam. Due to the different orientations of the defects, field distribution in each defect has different polarization directions. The arrows in the upper right inset represent the polarization state of the cavity mode, indicating the homogeneously distributed polarization. The bottom right inset indicates that the optical field penetrates mainly from the cavity in the $\Gamma - K$ directions of the Brillouin zone.

To verify the generated CV beam, we numerically calculated the far-field radiation patterns of the resonance mode using the Sommerfeld diffraction integral[18],

$$\boldsymbol{E}(x,y,z) = \frac{1}{2\pi}\nabla \times \iint \boldsymbol{n} \times \boldsymbol{E}_0(x_0,y_0,z_0)\frac{\exp(ikR)}{R}\mathrm{d}S, \tag{1}$$

where $\boldsymbol{E}_0(x_0,y_0,z_0)$ is the near field in the PPC cavity, $\nabla = \partial/\partial x\hat{e}_x + \partial/\partial y\hat{e}_y + \partial/\partial z\hat{e}_z$, $R = ((x-x_0)^2 + (y-y_0)^2 + (z-z_0)^2)^{1/2}$, and $\boldsymbol{n}$ is the unit vector in the z direction. Figure 1(c) shows the calculated far-field intensity profile, where the white arrows denote the polarization directions. Due to the symmetric polarization distributions and step-phase structures of the cavity mode, the far-field radiation pattern presents a ring-shaped intensity distribution. The hollow-core intensity indicates a polarization singularity at the center. The phase distributions of right-handed ($\text{RH} = E_x + iE_y$) and left-handed ($\text{LH} = E_x - iE_y$) circular polarization components are plotted in Figs. 1(d) and 1(e), respectively. The phases of the two components have opposite helical structures with a variation of 2π over around the central phase singularity. According to superposition principle[13], we can derive the electric-field expression of the PPC cavity mode as $E = A(-\sin\psi\,\boldsymbol{e}_x + \cos\psi\,\boldsymbol{e}_y)$, which is exactly an expression of standard azimuthal vector fields with the topological charge of 1. Here, A is the uniform amplitude, ψ denotes the azimuthal angle, and $\boldsymbol{e}_x$ and $\boldsymbol{e}_y$ are the corresponding orthogonal base vectors. Here, radially polarized CV beams cannot be generated in the PPC cavity due to the constraints of Bloch modes and the band structure.

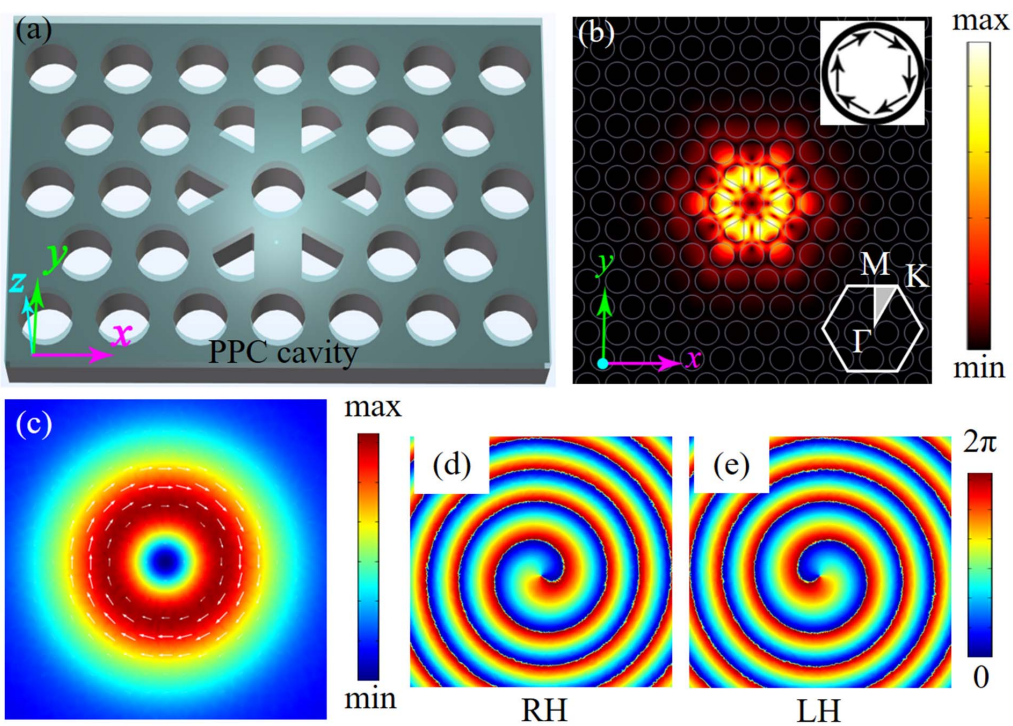

Fig. 1. (a) Schematic of the silicon PPC cavity with six cutting air holes for generating the CV beam. (b) Intensity distribution of the cavity mode. The upper right inset depicts the polarization directions of the field, and the bottom right hexagon depicts the Brillouin zone of the PPC slab. (c) Far-field intensity distribution of the generated CV beam; the white arrows denote the polarization directions. (d), (e) Phase diagrams of right-handed and left-handed circular polarization components of the CV beam.

3. Manipulating Far Field of PPC Cavity Mode by the Integrated SRR

In our previous work, we demonstrated that the integration of a plasmonic SRR on a PPC cavity could modify their resonance modes strongly, including the resonance line shapes and mode distributions. It could be attributed to the effective near-field coupling between the resonance modes in the two nanoresonators. Here, we would illustrate the SRR integrated on the PPC cavity could also be employed to modify the far-field radiation of the resonance mode in the PPC cavity, which could provide a strategy to control the polarization of the generated CV beam. As shown in Fig. 2(a), a gold (Au) SRR is integrated on a D-type PPC cavity to form a hybrid cavity[20]. The gap opening direction of the SRR has an orientation angle of φ with respect to the cutting direction of the D-type air hole. A silicon dioxide (SiO_2) buffering layer with a thickness of 100 nm is sandwiched between the PPC cavity and the SRR to avoid the destructive perturbations[22,23]. As shown in Fig. 2(b), a vector electric field with the polarization along the positive and negative directions of the y axis is generated in the resonance mode of the D-type PPC cavity. Under the excitation of this vector electric field, opposite charges are generated on the two arms of the integrated SRR, resulting in an electric dipole moment $\boldsymbol{p}$ in the x direction. The toroidal current in the SRR (represented by the white arrows) will generate a magnetic dipole moment $\boldsymbol{m}$ along the z direction. Under the coupling of these two eigenmodes, the scattered power of the far field can be defined by Larmor's formula as

$$P = \frac{4\pi}{3Z} k^4 (|\boldsymbol{p}|^2 + |\boldsymbol{m}|^2), \tag{2}$$

where Z is the impedance of the surrounding medium, and k is the wave vector[24]. $\boldsymbol{p}$ and $\boldsymbol{m}$ are induced by the electric field $\boldsymbol{E}_{\mathrm{PPC}}$ and magneticfield $\boldsymbol{H}_{\mathrm{PPC}}$ in the D-type PPC cavity and can be written as[25]

$$\begin{pmatrix} \boldsymbol{p} \\ \boldsymbol{m} \end{pmatrix} = \frac{1}{2}\boldsymbol{\alpha}_{\mathrm{SRR}} \begin{pmatrix} \boldsymbol{E}_{\mathrm{PPC}} \\ \boldsymbol{H}_{\mathrm{PPC}} \end{pmatrix} = \frac{1}{2}\alpha(\omega) \begin{pmatrix} \eta_E & 0 & 0 & 0 & 0 & i\eta_C \\ 0 & 0 & 0 & 0 & 0 & 0 \\ 0 & 0 & 0 & 0 & 0 & 0 \\ 0 & 0 & 0 & 0 & 0 & 0 \\ 0 & 0 & 0 & 0 & 0 & 0 \\ -i\eta_C & 0 & 0 & 0 & 0 & \eta_H \end{pmatrix}$$

$$\cdot \begin{pmatrix} E^x_{\mathrm{PPC}} \\ E^y_{\mathrm{PPC}} \\ E^z_{\mathrm{PPC}} \\ E^x_{\mathrm{PPC}} \\ E^y_{\mathrm{PPC}} \\ E^z_{\mathrm{PPC}} \end{pmatrix} = \frac{\omega_0^2 V_0}{2(\omega_0^2 - \omega^2 - i\omega\gamma)} \begin{pmatrix} \eta_E \cdot E^x_{\mathrm{PPC}} + i\eta_C \cdot H^z_{\mathrm{PPC}} \\ 0 \\ 0 \\ 0 \\ 0 \\ -i\eta_C \cdot E^x_{\mathrm{PPC}} + \eta_H \cdot H^z_{\mathrm{PPC}} \end{pmatrix}, \tag{3}$$

where $\boldsymbol{\alpha}_{\mathrm{SRR}}$ is the polarizability tensor determined by the coupling efficiency and Lorentzian factor $\alpha(\omega) = \omega_0^2/(\omega_0^2 - \omega^2 - i\omega\gamma)$, ω_0 is the resonance frequency of the SRR, γ is the damping rate due to the Ohmic loss of Au, and V_0 is the physical particle volume. η_E and η_H are the electric and magnetic field coupling efficiency, respectively, and η_C refers to the electromagnetic cross coupling efficiency. Equation (3) indicates that the polarization of the far field from the hybrid SRR-PPC cavity is dominantly perpendicular to the gap direction of the SRR, and the intensity is proportional to the coupling efficiency.

Figures 2(c)–2(g) show the calculated far-field intensity profiles of the SRR-PPC cavity mode as the SRR is rotated in-plane relative to the center of the PPC cavity, i.e., the angle φ varying from 0° to 180°. With the SRR, the far-field radiation of the resonance mode of the D-type PPC cavity shows a constriction distribution with an elliptical shape. For different SRR opening directions, the long axis of the elliptical far-field distribution changes, which is consistent with the gap opening direction of the SRR. It indicates that the far field of the hybrid cavity is dominated by the eigenmode of the electric dipole of the SRR. In addition, the polarization direction of the far field is perpendicular to the gap direction of the SRR. As a result, the integrated SRR could control the polarization and field distribution of the far-field scattering of the PPC cavity.

Note that the far-field scattering intensities from the hybrid cavity change as well when the SRR is rotated in different directions. It could be attributed to the angle dependence of the coupling efficiency between the SRR mode and PPC cavity mode. In general, the couple efficiency $\eta(\varphi)$ can be calculated by[26]

$$\eta(\varphi) = \frac{\iiint_{\mathrm{SRR}} (\mu_0 |\boldsymbol{H}_{\mathrm{hyb}}|^2 + \varepsilon_0 |\boldsymbol{E}_{\mathrm{hyb}}|^2) \mathrm{d}V}{\iiint_{+\infty}^{-\infty} (\mu_0 |\boldsymbol{H}_{\mathrm{hyb}}|^2 + \varepsilon_0 |\boldsymbol{E}_{\mathrm{hyb}}|^2) \mathrm{d}V}, \tag{4}$$

where μ_0 and ε_0 are the vacuum permeability and permittivity, and $\boldsymbol{H}_{\mathrm{hyb}}$ and $\boldsymbol{E}_{\mathrm{hyb}}$ represent the magnetic and electric field of the hybrid SRR-PPC cavity mode, respectively. The calculated couple efficiency and far-field scattering intensity using the finite-element method are shown in Fig. 3. As expected, the efficiency is dependent on the opening angle of the SRR and is proportional to the far-field scattering intensity.

4. Controlling the Polarization of CV Beams

The nano-antenna effect of the SRR over the far field of the PPC cavity could be further employed to control the CV beam generated from the PPC cavity shown in Fig. 1, which has six defects of cutting air holes. As illustrated in Fig. 4(a), six SRRs are symmetrically integrated on top of the six defects of the PPC cavity to form a hybrid cavity. All of the six SRRs have the same orientation angle with respect to the radial direction of the PPC cavity, which would be rotated by an angle of φ simultaneously. The eigenmode of the SRRs couples with the CV mode of the PPC cavity in the near field and controls the far-field radiation. Figure 4(b) presents the far-field scattering spectra of the coupled modes from the hybrid SRR-PPC cavity. Compared

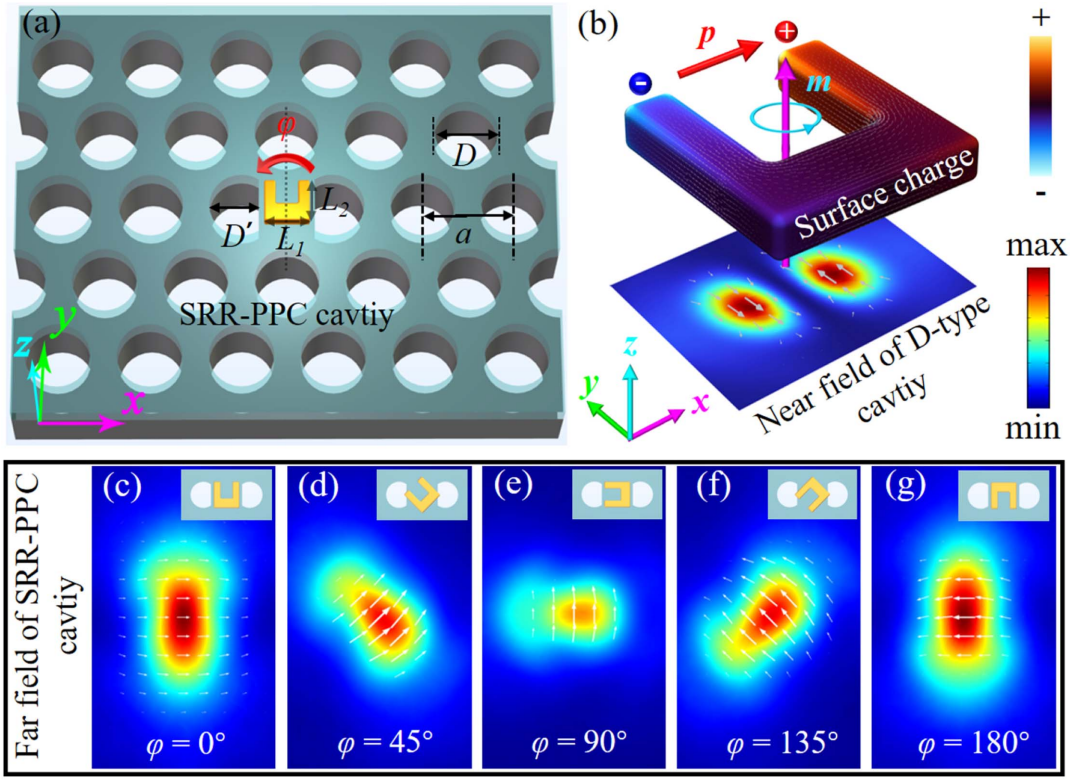

Fig. 2. (a) Schematic of the hybrid cavity with an Au SRR covered on a D-type PPC cavity. The silicon PPC slab (refractive index $n = 3.37$) has a thickness of $t = 220$ nm and lattice constant of $a = 370$ nm, the diameter of the air-holes is $D = 0.34a$, and the cutting air holes have a width of $D' = 0.8D$. Geometrical parameters of the SRR: arm length $L_1 = 130$ nm and $L_2 = 140$ nm; arm width $w = 27.5$ nm; thickness $d = 35$ nm; gap distance between two arms $g_x = 75$ nm; gap depth $g_y = 90$ nm. The black dash denotes the cutting direction of the PPC cavity. (b) Surface charge distribution of the SRR as it couples with the PPC cavity. The bottom is the calculated near field of the PPC cavity (at $z = 100$ nm above the PPC slab), where gray arrows indicate the polarization directions. (c)–(g) Far-field intensity distributions of the hybrid SRR-PPC cavity (at $z = 5$ μm above the SRR) with the SRR opening along different directions, where white arrows represent the polarization directions. The upper right inset depicts the schematic of the SRR with different orientation angles, respectively.

with the pure PPC cavity without the SRRs, resonance peaks with obvious Fano line shapes are observed in the hybrid cavity. The origin of this Fano-like behavior comes from an effective coupling between the narrowband resonance mode of the PPC cavity and the broadband resonance mode of the SRR[27]. The frequency shift of the resonance peak indicates that the effective permeability of the SRR changes with the increase of the orientation angle[28]. Although the Q factor decreases from 1089 to 86 after the integration of SRRs, the mode volume V_m is also reduced from $0.72(\lambda/n_{\text{slab}})^3$ to $0.047(\lambda/n_{\text{slab}})^3$, resulting in a higher Q/V_m ratio compared to the bare PPC cavity. The detailed results for different orientation angles are provided in the Table 1. With the increasing angle φ, the resonance spectra show blueshift, revealing the perturbation in permittivity and permeability caused by the electromagnetic interaction. Figures 4(c)–4(f) show the calculated far-field intensity profiles with φ varying from 0° to 90°. One can see that the polarization of the CV beam gradually changes from azimuthal distribution to radial distribution. The profile of the beam increases and gradually becomes a hexagonal shape, which is attributed to the scattering caused by the weakened coupling between the SRRs and PPC cavity.

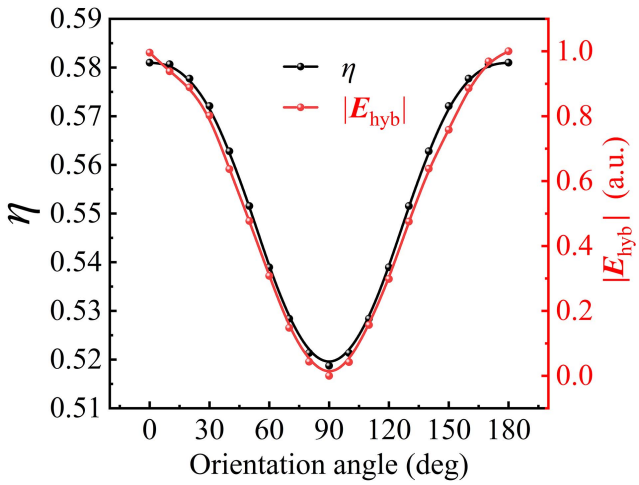

Fig. 3. Calculated coupling efficiency and far-field scattering intensity as a function of the orientation angle φ.

The difference of the far-field intensity profiles obtained from the SRR-PPC cavity with different SRR gap directions also implies a change of the collection efficiency for the CV beams.

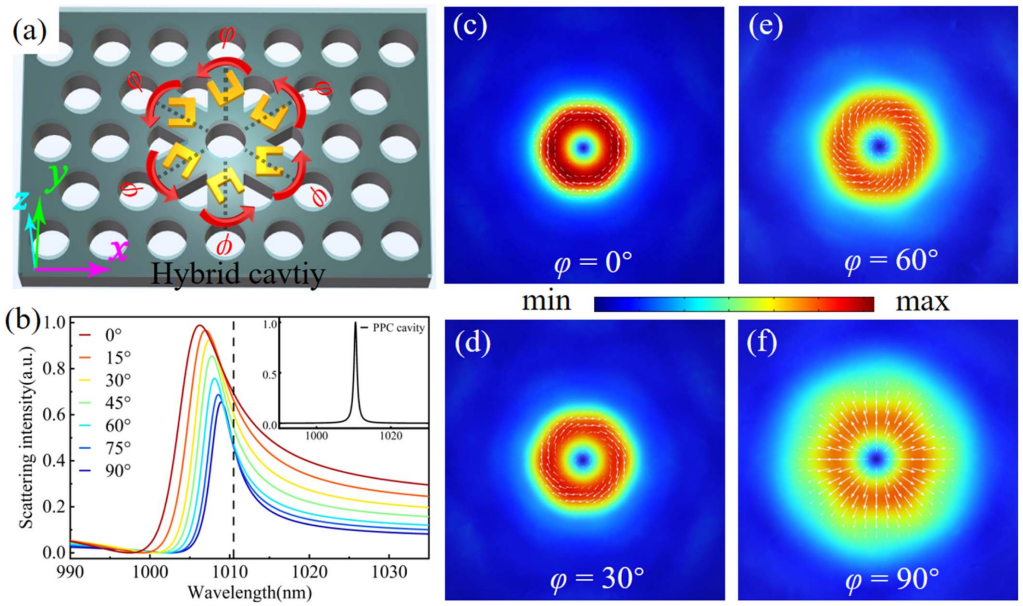

Fig. 4. (a) Schematic of the SRR-PPC hybrid cavity for generating CV beams with tailorable polarization; (b) calculated emission spectra of CV mode from the SRR-PPC cavity with the orientation angle φ varying from 0° to 90°; the dashed line denotes the resonance wavelength of the CV mode in the PPC cavity without SRR, whose emission spectrum is shown in the inset. (c)–(f) Calculated far-field intensity distributions (at $z = 5$ μm above the SRR) of the CV beams. The arrows denote the polarization directions.

Table 1. Calculated Q Factor, Mode Volume V_m, and Q/V_m before and after the Integration of SRRs.

φ	Q	$V_m(\lambda/n_{\text{slab}})^3$	Q/V_m
PPC without SRRs	1089	0.721	1512.5
0°	86	0.047	1829.8
30°	140.9	0.061	2309.8
60°	199.2	0.061	3265.6
90°	235	0.055	4272.7

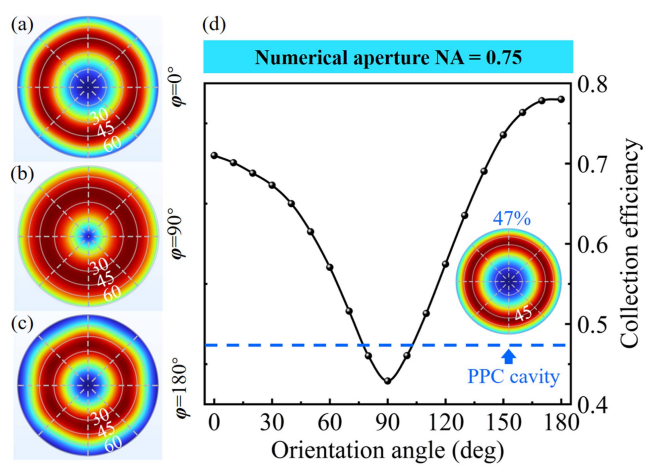

Fig. 5. (a)–(c) Far-field angular distributions of the SRR-PPC cavity mode for φ = 0°, 90°, and 180°, respectively; (d) calculated collection efficiency as a function of φ; blue dashed line marks the value of collection efficiency of the PPC cavity without SRRs; inset shows the far-field angular distribution of the CV mode in the PPC cavity without SRRs.

To characterize the relationship between the collection efficiency and orientation angle of the SRRs, we calculate the far-field angular distributions of the cavity mode at different φ and display them with the field distribution over the regions in different divergence angles, as shown in Figs. 5(a)–5(c). Compared with the far-field mode in the pure PPC cavity without SRRs shown in the inset of Fig. 5(d), the field intensity is mainly confined near the divergence angle of 45°. Especially when $\varphi = 180°$, most of the power is concentrated between the divergence angles of 30° and 45°, indicating a significant increase in collection efficiency for an objective lens with moderately small numerical aperture (NA). The high efficiency is beneficial for the coupling of the CV beams to an optical objective lens, which reduces the requirement for additional integration of other optical components. The high-efficiency free-space coupling of the CV beam could also facilitate applications in free-space communication, high-resolution imaging, and optical manipulations by the chip-generated CV beam. Figure 5(d) shows the calculated collection efficiency as a function of φ for the objective lens with NA = 0.75. The collection efficiency of CV beam reaches the highest value of 78% when $\varphi = 180°$, which is higher than 71% when $\varphi = 0$. The discrepancy is attributed to the different coupling efficiency η_C between two eigenmodes of the SRR. When $\varphi = 180°$, the magnetic dipole and

electric dipole of the SRR couple to each other strongly due to the variation of the near field in the PPC cavity, which results in a smaller divergence angle of the far-field radiation. The lowest collection efficiency of 43% can be obtained when $\varphi = 90°$ due to the insufficient coupling between the SRRs and PPC cavity. As a comparison, the collection efficiency of the PPC cavity without the SRRs always equals 47%.

5. Conclusion

In conclusion, we have demonstrated the generation of CV beams with tailored polarization from a PPC cavity by integrating plasmonic SRRs. The PPC cavity, with six cutting air holes, forms radially symmetric structure defects and supports resonance mode with azimuthal polarization. By aligning six SRRs on the six defects of the PPC cavity, the azimuthally polarized CV beam is transformed into the radially polarized CV beam. Compared with the CV beam generated from the pure PPC cavity, the collection efficiency of the CV beam generated from the SRR-PPC cavity is significantly improved, which is favorable for a CV beam generated from the on-chip SRR-PPC cavity in free-space applications, such as optical communications, imaging, and nonlinear optics[29–31].

Acknowledgement

This work was supported by the National Key Research and Development Program of China (Nos. 2022YFA1404800 and 2017YFA0303800), the National Natural Science Foundation of China (Nos. 91950119, 61905196, and 62105263), the Key Research and Development Program in Shaanxi Province of China (No. 2020JZ-10), and the Fundamental Research Funds for the Central Universities (Nos. 310201911cx032, 3102019JC008, and 310202011qd002).

References

1. M. A. Ahmed, A. Voss, M. M. Vogel, and T. Graf, "Multilayer polarizing grating mirror used for the generation of radial polarization in Yb:YAG thin-disk lasers," Opt. Lett. **32**, 3272 (2007).
2. J. Mun, S.-W. Moon, and J. Rho, "Multipole decomposition for interactions between structured optical fields and meta-atoms," Opt. Express **28**, 36756 (2020).
3. A. Peinado, A. Turpin, C. Iemmi, A. Márquez, T. K. Kalkandjiev, J. Mompart, and J. Campos, "Interferometric characterization of the structured polarized light beam produced by the conical refraction phenomenon," Opt. Express **23**, 18080 (2015).
4. Y. Senatsky, J. F. Bisson, J. Li, A. Shirakawa, M. Thirugnanasambandam, and K. Ichi Ueda, "Laguerre-Gaussian modes selection in diode-pumped solid-state lasers," Opt. Rev. **19**, 201 (2012).
5. N. Livakas, E. Skoulas, and E. Stratakis, "Omnidirectional iridescence via cylindrically polarized femtosecond laser processing," Opto-Electronic Adv. **3**, 190035 (2020).
6. F. Xiao, W. Shang, W. Zhu, L. Han, M. Premaratne, T. Mei, and J. Zhao, "Cylindrical vector beam-excited frequency-tunable second harmonic generation in a plasmonic octamer," Photonics Res. **6**, 157 (2018).
7. S. A. Maier, *Plasmonics Fundamentals and Applications* (Springer, 2007).
8. A. de las Heras, A. K. Pandey, J. S. Román, J. Serrano, E. Baynard, G. Dovillaire, M. Pittman, C. G. Durfee, L. Plaja, S. Kazamias, O. Guilbaud, and C. Hernández-García, "Extreme-ultraviolet vector-vortex beams from high harmonic generation," Optica **9**, 71 (2022).
9. I. Nape, N. Mashaba, N. Mphuthi, S. Jayakumar, S. Bhattacharya, and A. Forbes, "Vector-mode decay in atmospheric turbulence: an analysis inspired by quantum mechanics," Phys. Rev. Appl. **15**, 034030 (2021).
10. X. Cai, J. Wang, M. J. Strain, B. Johnson-Morris, J. Zhu, M. Sorel, J. L. O'Brien, M. G. Thompson, and S. Yu, "Integrated compact optical vortex beam emitters," Science **338**, 363 (2012).
11. S. A. Schulz, T. Machula, E. Karimi, and R. W. Boyd, "Integrated multi vector vortex beam generator," Opt. Express **21**, 16130 (2013).
12. Y. Kozawa and S. Sato, "Optical trapping of micrometer-sized dielectric particles by cylindrical vector beams," Opt. Express **18**, 10828 (2010).
13. Y. Lu, Y. Xu, X. Ouyang, M. Xian, Y. Cao, K. Chen, and X. Li, "Cylindrical vector beams reveal radiationless anapole condition in a resonant state," Opto-Electronic Adv. **5**, 210014 (2022).
14. X. T. Gan, C. Y. Zhao, S. Q. Hu, T. Wang, Y. Song, J. Li, Q. H. Zhao, W. Q. Jie, and J. L. Zhao, "Microwatts continuous-wave pumped second harmonic generation in few- and mono-layer GaSe," Light Sci. Appl. **7**, 17126 (2018).
15. B. Shi, Y. Cao, T. Zhu, H. Li, Y. Zhang, R. Feng, F. Sun, and W. Ding, "Multiparticle resonant optical sorting using a topological photonic structure," Photonics Res. **10**, 297 (2022).
16. L. Wu, X. Jiang, J. Zhao, W. Liang, Z. Li, W. Huang, Z. Lin, Y. Wang, F. Zhang, and S. Lu, "MXene-based nonlinear optical information converter for all-optical modulator and switcher," Laser Photonics Rev. **12**, 1800215 (2018).
17. M. Burresi, R. J. P. Engelen, A. Opheij, D. Van Oosten, D. Mori, T. Baba, and L. Kuipers, "Observation of polarization singularities at the nanoscale," Phys. Rev. Lett. **102**, 033902 (2009).
18. K. Kitamura, K. Sakai, N. Takayama, M. Nishimoto, and S. Noda, "Focusing properties of vector vortex beams emitted by photonic-crystal lasers," Opt. Lett. **37**, 2421 (2012).
19. C. Zhao, X. Gan, S. Liu, Y. Pang, and J. Zhao, "Generation of vector beams in planar photonic crystal cavities with multiple missing-hole defects," Opt. Express **22**, 9360 (2014).
20. K. Chang, L. Fang, C. Zhao, J. Zhao, and X. Gan, "Cylindrical vector resonant modes achieved in planar photonic crystal cavities with enlarged air-holes," Opt. Express **25**, 21594 (2017).
21. R. D. M. J. D. Joannopoulos, S. G. Johnson, and J. N. Winn, *Photonic Crystals: Molding the Flow of Light*, 2nd ed. (Princeton, 2007).
22. I. Cestier, D. Gready, U. Ben-Ami, G. Eisenstein, S. Combrie, Q. Tran, and A. de Rossi, "Near field imaging of a GaAs photonic crystal cavity and waveguide using a metal coated fiber tip," Opt. Express **17**, 15274 (2009).
23. L. K. M. Burresi, T. Kampfrath, D. van Oosten, J. C. Prangsma, B. S. Song, and S. Noda, "Magnetic light-matter interactions in a photonic crystal nanocavity," Phys. Rev. Lett. **105**, 123901 (2010).
24. P. Kumar, C. Prakash, O. P. Thakur, R. Chatterjee, and T. C. Goel, "Dielectric, ferroelectric and pyroelectric properties of PMNT ceramics," Phys. B **371**, 313 (2006).
25. I. Sersic, C. Tuambilangana, T. Kampfrath, and A. F. Koenderink, "Magnetoelectric point scattering theory for metamaterial scatterers," Phys. Rev. B **83**, 245102 (2011).
26. Q. Yuan, L. Fang, Q. Zhao, Y. Wang, B. Mao, V. Khayrudinov, H. Lipsanen, Z. Sun, J. Zhao, and X. Gan, "Mode couplings of a semiconductor nanowire scanning across a photonic crystal nanocavity," Chin. Opt. Lett. **17**, 062301 (2019).
27. M. F. Limonov, M. V. Rybin, A. N. Poddubny, and Y. S. Kivshar, "Fano resonances in photonics," Nat. Photon. **11**, 543 (2017).
28. Y. Ji, B. Wang, L. Fang, Q. Zhao, F. Xiao, and X. Gan, "Exciting magnetic dipole mode of split-ring plasmonic nano-resonator by photonic crystal nanocavity," Materials **14**, 7330 (2021).
29. M. Smit, J. van der Tol, and M. Hill, "Moore's law in photonics," Laser Photonics Rev. **6**, 1 (2012).
30. S. H. Bae, H. Kum, W. Kong, Y. Kim, C. Choi, B. Lee, P. Lin, Y. Park, and J. Kim, "Integration of bulk materials with two-dimensional materials for physical coupling and applications," Nat. Mater. **18**, 550 (2019).
31. P. K. Tien, "Integrated optics and new wave phenomena in optical waveguides," Rev. Mod. Phys. **49**, 361 (1977).